applied optics

Ground flat-field calibration of a space astronomical telescope using a spatial time-sharing calibration method

Jianing Zheng,[1,2] Xu He,[1,3] Ning Zhang,[1] Jingtian Xian,[1,2] and Xiaohui Zhang[1,*]

[1]Changchun Institute of Optics, Fine Mechanics and Physics, Chinese Academy of Sciences, Changchun 130033, China
[2]Graduate University of the Chinese Academy of Sciences, Beijing 10039, China
[3]hexu_ciomp@sina.com
*zhangxiaohui0123@163.com

Received 30 June 2023; revised 26 September 2023; accepted 27 September 2023; posted 28 September 2023; published 12 October 2023

Preflight ground flat-field calibration is significant to the development phase of space astronomical telescopes. The uniformity of the flat-field illumination reference source seriously decreases with the increasing aperture and the telescope's field of view, directly affecting the final calibration accuracy. To overcome this problem, a flat-field calibration method that can complete calibration without a traditional flat-field illumination reference source is proposed on the basis of the spatial time-sharing calibration principle. First, the characteristics of the flat field in the spatial domain taken by the space astronomical telescope are analyzed, and the flat field is divided into large-scale flat (L-flat) and pixel-to-pixel flat (P-flat). They are then obtained via different calibration experiments and finally combined with the data fusion process. L-flat is obtained through star field observations and the corresponding L-flat extraction algorithm, which can obtain the best estimation of L-flat based on numerous photometry samples, thereby effectively improving calibration accuracy. The simulation model of flat-field calibration used for accuracy analysis is established. In particular, the error sources or experimental parameters that affect the accuracy of L-flat calibration are discussed in detail. Results of the accuracy analysis show that the combined uncertainty of the proposed calibration method can reach 0.78%. Meanwhile, experiments on an optic system with a Φ142 mm aperture are performed to verify the calibration method. Results demonstrate that the RMS values of the residual map are 0.720%, 0.565%, and 0.558% at the large-, middle-, and small-scale, respectively. The combined calibration uncertainty is 0.88%, which is generally consistent with the results of the accuracy analysis.

https://doi.org/10.1364/AO.498846

1. INTRODUCTION

Ground flat-field calibration, which aims to correct the radiation response variations within the entire optical path, is crucial to the development phase of space astronomical telescopes [1–3]. According to the calibration plan, flat-field calibration can be divided into ground laboratory and on-orbit flat-field calibration [4]. Data obtained from ground flat-field calibration are significant flat-field references in the early on-orbit operation phase [5,6], especially the high-quality monochromatic flat fields that are difficult to obtain directly by star field observation. A sufficient ground test can greatly reduce the commissioning time and operation risk of the instrument during the postlaunch phase.

Ground flat-field calibration commonly demands a flat-field illumination reference source that covers the field of view (FOV) and aperture of the telescope [7,8]. The commonly adopted approaches use an integrating sphere light source or flat-field screen illumination as the reference source [9–12]. The integrating sphere light source can achieve excellent radiance uniformity at the sphere orifice, but a large-aperture integrating sphere would greatly enhance the manufacturing costs and increase difficulties as the telescope aperture increases. Taking the 2 m orifice diameter of the integrating sphere as an example, the required diameter of the sphere should reach 4.47 m to achieve the expected radiance uniformity. As a result, this poses a challenge to manufacturing and heat dissipation control. The Dark Energy Survey Camera, Panoramic Survey Telescope, and Rapid Response System use reflective and transmissive flat-field screen illumination, respectively [11,12]. However, given stray-light effects and the physical properties of the screen, the total uncertainty is 5% for the reflective method and 7.3% for the transmission method. In addition, most space telescopes need a low-temperature environment to obtain high signal-to-noise ratio (SNR) data; the calibration test thus has to be completed under vacuum and in a cold black environment [9,13]. As a

result, the environmental adaptability problem of the flat-field illumination reference source becomes fairly complicated.

To eliminate the dependence on the illumination reference source, the Large Synoptic Survey Telescope uses a subaperture collimated beam projector to build a star field and then completes the measurement of the low- to midspatial frequency flat field [14–16]. This method does not suffer from stray-light effects or the reflections (known as ghosting) present when using flat-field illumination. When calibrating the Kepler space telescope, the flat-field model includes large-scale geometric and small-scale (pixel-to-pixel) flats [17–19], where small-scale flats are obtained through a source that uniformly illuminates the detector during ground tests. For large-scale flats, an additional on-orbit calibration plan of star field observations is needed. The results show that the local flat calibration accuracy is 0.96% [19]. Hubble Space Telescope Wide Field Camera 3 obtains flat-field reference files by the CASTLE optical stimulus during the ground test [4,20]. However, it is during the post-launch commissioning phase that the final high-precision flat fields are obtained, via additional low-frequency residual correction based on Omega Centauri observation data. The James Webb Space Telescope Near-Infrared Spectrograph separates the optical path into three manageable components [1,21], each with a dedicated set of flat-field references: fore optics flat (F-flat); spectrograph flat (S-flat); and detector flat (D-flat); where F-flat is measured during the postlaunch commissioning of the instrument based on star field observation data, while the others are measured during ground tests.

L-flat indicates the large-scale difference in radiation response [20]. Generally, the accuracy of the final flat field is closely related to the L-flat calibration procedure. L-flat calibration can be performed by star field observations, in which the main principle is to extract the L-flat through the photometry difference of the same star at different positions of the detector. When the star sample size increases and the background noise of the star field decreases, the accuracy and robustness of the L-flat extraction algorithm adopting the optimal estimation principle remarkably improves. Therefore, a spatial time-sharing calibration method is proposed. In this method, L-flat and P-flat are obtained independently and combined with the data fusion procedure. Given that the L-flat calibration method only focuses on the photometry difference of a single star, each star in the star field can therefore have a different flux, thereby removing the dependence on a uniform illumination reference source. The results of the accuracy analysis and validation experiment demonstrate the effectiveness of the proposed method. The combined calibration uncertainty is 0.88%. Compared with the general accuracy (approximately 5%) of the ground flat-field calibration of an astronomical telescope [12], the proposed method can greatly improve the calibration accuracy.

The rest of this paper is organized as follows: Section 2 introduces the overall scheme of the calibration method, including the data processing algorithm. Section 3 presents the established simulation model and the analysis of the error source or parameter configuration affecting the L-flat calibration accuracy in detail. Section 4 discusses the experiment conducted to verify the method described above. Finally, the conclusions are presented in Section 5.

2. SPATIAL TIME-SHARING CALIBRATION PRINCIPLE

A. Flat-Field Characteristics

Flat-field accounts for the variation in throughput along the entire optical path, i.e., from the observatory primary mirror to the instrument detector subsystem, for a conventional space astronomical telescope [1]. As mentioned, the flat field can generally be divided into a global large-scale (L-flat) and local pixel-to-pixel (P-flat) in the spatial domain. Specifically, L-flat is mainly caused by the nonuniform transmission of light along the optical systems, such as the throughput losses caused by dust and the roughness of the optical mirror, the image field bending of the exit pupil surface of the optical system, stray light, and the inconsistent response of different detectors. P-flat is solely determined by the properties of the detector subsystem, such as the conversion from photons to electrons and the ultimate count rate [2].

In general, P-flat and L-flat are introduced by the entire optical path of the telescope and dominated by two independent components. This characteristic leads to the difference and complementarity between the two flats, which also indicate that the spatial time-sharing calibration method is feasible. Hence, P-flat and L-flat calibration methods, together with the corresponding data processing algorithms, are proposed; then, the final flat field is obtained through data fusion.

B. P-Flat Calibration

1. P-Flat Calibration Method and Equipment

As noted, generally no small-scale variations occur in the reflectivity along the light paths; hence, selecting the detector pixelwise flat field as the P-flat is safe. In practice, the calibration test of a ground detector flat field has high accuracy [9]. Therefore, P-flat calibration would not considerably improve the final calibration accuracy and is not the main content of this study. A uniform extended illumination that covers the detector area is used to acquire flat field images. A diagram of the P-flat calibration configuration is shown in Fig. 1.

Given the influence of the internal baffle, geometric position of the light source, and heat factor at the spherical orifice, the center of the spherical orifice is not the best position for measurement. Generally, the detector is placed at a certain distance from the integrating sphere, ensuring that the detector surface is parallel to the orifice. The shading dark box placed outside the whole P-flat calibration equipment is also used to reduce stray-light effects.

Additionally, given that the pixel-level P-flat coefficient is bias subtracted, an additional set of bias images with the shortest exposure time is needed.

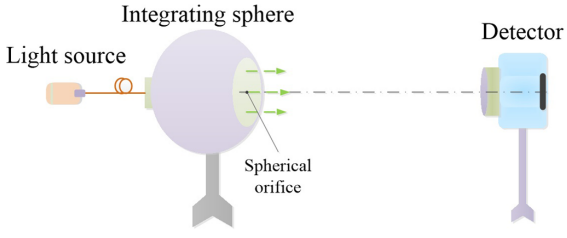

Fig. 1. Diagram of the P-flat calibration configuration.

2. P-Flat Data Processing Algorithm

P-flat is obtained by performing bias subtraction and normalization processes on the detector-wise flat-field images. The central region of 100 × 100 pixels is selected for the normalization process. All the images collected during the measurement with multiple shootings must be averaged first to improve the SNR of the images.

C. L-Flat Calibration

1. L-Flat Calibration Method and Equipment

When a star field in which each star has a constant brightness is observed with a telescope, the measured flux differences for the same star at different positions within the detector determine the L-flat structure [20,21]. On the basis of this principle, we designed the L-flat calibration method. First, the star field source is constructed and imaged multiple times at different positions. Then, the star photometry data containing star ID, photometry value (in analog-to-digital unit, ADU), and position and photometry errors are calculated and further used to extract the final L-flat. It is worth remembering that different stars can vary in brightness, as the measured flux differences are for the same star. Therefore, this method does not require the strict brightness uniformity of the star field source, but the brightness of a star must be highly stable during measurement. A diagram of the L-flat calibration configuration is shown in Fig. 2.

The calibration equipment consists of a small aperture integrating sphere, light source, multipinhole mask, and collimator. The collimator should cover the aperture of the telescope. Here, the light source is consistent with that in the P-flat calibration configuration. The multipinhole mask is placed at the focal plane of the collimator to construct the star field source. A 2D turntable is used to realize the orientations' adjustment of the telescope. Meanwhile, a calibrated silicon photodiode is used at the exit of the collimator to correct the radiation variations during measurement. The multipinhole mask determines the shape of the star on the focal plane of the telescope. Furthermore, the physical size of the pinholes is determined by the balance of photometry accuracy and star field density. Specific details on the pinhole size will be discussed later. It should be emphasized that the images collected by the detector have no interference because the light emitted by the integrating sphere is incoherent.

2. L-Flat Extraction Algorithm

L-flat can be expanded as a linear sum of 2D basis functions. In addition, flux differences between measurements for the same star at different positions of the detector constrain the coefficients of the linear sum. This reduces mathematically to an overdetermined linear least-squares problem. Here, L-flat is represented as a set of 2D chessboard grid of basis functions of varying order [4]. The original images used for data processing include star field images of different observations, detector-wise flat-field images, and bias images. The algorithm flow is shown in Fig. 3.

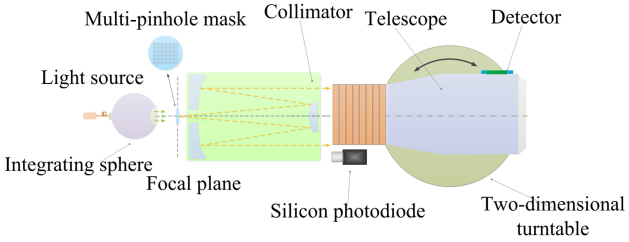

Fig. 2. Diagram of L-flat calibration configuration.

1. Image preprocessing: Similar to astronomical images, star field images must first undergo the following image preprocessing steps, namely, bias subtraction, flat-field correction based on the detector-wise flat field, and gain correction of the detector. Through the above steps, most of the detector effects on star photometry are removed, which is important for the subsequent data fusion procedure.
2. Background estimation: To detect faint stars and accurately measure their fluxes, we first construct a background map and then remove the influence of background noise on photometry. Given the relatively uniform and sparse distribution of holes in the multi-pinhole mask used in our method, a method similar to the DAOPHOT program is used [22]. Briefly, background map is derived by computing the σ-clipped median of the local background in each mesh of the grid first. Bilinear interpolation between the meshes of the grid is then applied on the resulting background map. A mesh with a width of 32–128 pixels is suitable.
3. Star detection: Threshold detection is appropriate in the absence of blending for stars in the star field, where the threshold is correlated with the local background deviation. In addition, barycenter coordinates are used to define the position of the "center" of a star.
4. Star photometry: The star flux above the background within a circular aperture is estimated by aperture photometry. The diameter of the aperture (in pixels) is related to the full width at half maximum (FWHM) of each star. Each "normal" pixel is subdivided into 5 × 5 subpixels before measuring the flux within the aperture. The flux uncertainty is computed using the following equation [23]:

$$\mathrm{e} = \sqrt{\sum_{i \in A} \left(\sigma_i^2 + \frac{p_i}{g} \right)}, \tag{1}$$

where A is the set of pixels defining the photometry aperture, σ_{i} denotes the standard deviation of the noise in the ADU unit estimated from the local background, p_{i} is the measurement image pixel value subtracted from the background, and g is the effective detector gain in e^{-}/ADU. The error estimate here considers the photon and detector noise.

Finally, the catalogs for each image are merged into a single master catalog, including a unique star ID, the image number, the detector position, and the flux and error.
5. L-flat extraction: Assuming that the flat field of telescope only has a low-frequency content (L-flat). In addition, the flat field $[R(x, y)]$ can be expanded as a linear sum of K 2D basis functions

$$R(x, y) = \sum_k a_k \cdot R_k(x, y), \quad (k = 1, 2, \ldots, K). \tag{2}$$

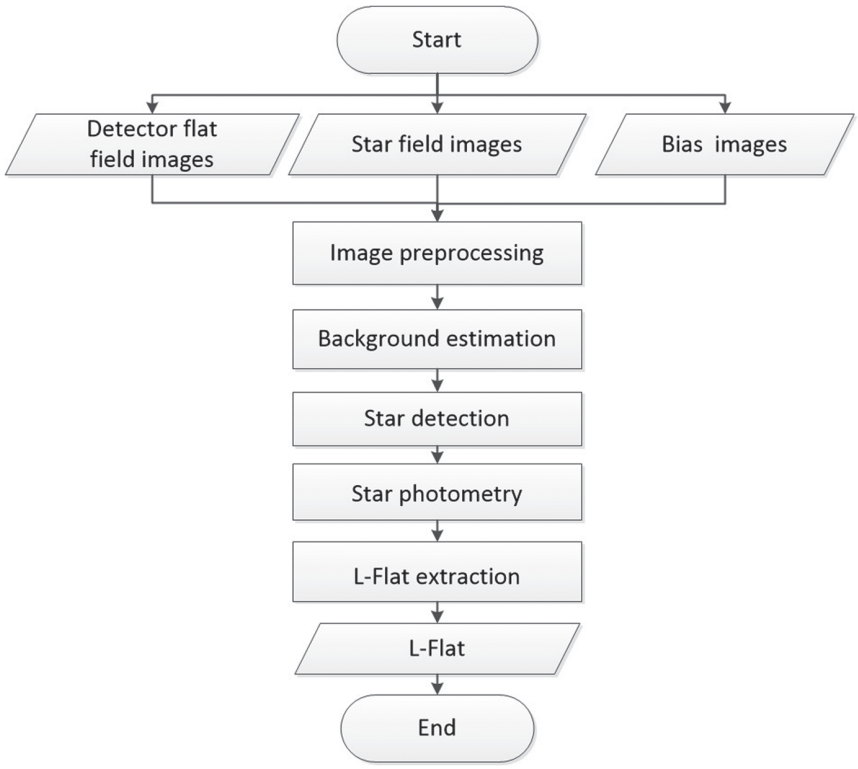

Fig. 3. L-flat extraction algorithm flow.

The form of the basis functions and k determine the L-flat characteristics. The chessboard form, which has independent solutions for each mesh of the grid, is used here:

$$R_k(x, y) = \begin{cases} 1, & \text{if } (x, y) \text{ in mesh} \\ 0, & \text{otherwise} \end{cases}. \tag{3}$$

The total number of basis functions is equal to the number of meshes divided from the detector: $K = W \times H$. Each mesh has a size of $(X/W) \times (Y/H)$.

The coefficients (a_k) that characterize the L-flat must be determined. Hence, star i, with unknown flux F_i, is considered; star i is observed $N_i \geq 1$ times. The telescope orientations are rotated between observations, so that, in each observation, the star falls on a different position (x_{ij}, y_{ij}) of the detector, where $j = 1, 2, \ldots, N_i$. For each star, aperture photometry is performed, obtaining star flux O_{ij} with errors (e_{ij}):

$$F_i + R(x_{ij}, y_{ij}) = O_{ij} \pm e_{ij},$$

$$(i = 1, 2, \ldots, S;\ j = 1, 2, \ldots, N_i) \tag{4}$$

Without loss of generality, $R(x, y)$ averages to zero over the detector:

$$\frac{1}{p}\sum_{p=1}^{P} R(x_p, y_p) = \sum_{k=1}^{K} a_k \sum_{p=1}^{P} R_k(x_p, y_p) = 0. \tag{5}$$

Here, the imaging position of point p on the detector is (x_p, y_p).

Equations (4) and (5) can be written as a linear matrix equation. As the number of unknowns is typically smaller than the number of constraints, the matrix equation is therefore overdetermined. Finally, an optimal L-flat function estimation is obtained through the least-squares method. In addition, bilinear interpolation and normalization are performed to make the L-flat size consistent with the image. The same central region of 100×100 pixels is selected as the normalization reference.

D. Spatial Data Fusion

Matrix multiplication of L-flat and P-flat in the spatial domain is used here to acquire the LP-flat:

$$\text{LP-Flat} = \text{L-Flat} \times \text{P-Flat}. \tag{6}$$

Here, the size of the matrix is consistent with that of the images collected by the detector. Finally, LP-flat is used as the final flat field reference file.

3. ACCURACY ANALYSIS

The calibration method can be summarized into three independent procedures, i.e., L-flat calibration, P-flat calibration, and spatial data fusion, and all these procedures together determine the final calibration accuracy. The P-flat calibration accuracy is mainly related to the calibration method and equipment. The P-flat calibration experiment in the laboratory shows that the calibration uncertainty can be controlled within 0.4% through a careful calibration procedure. The accuracy of L-flat calibration is affected not only by the calibration method and equipment but also by the L-flat data processing algorithm,

which is thus the main content of accuracy analysis. Next, this study focuses on the error traceability paths of L-flat calibration.

A. Accuracy of L-Flat Calibration

L-flat calibration accuracy depends on the quality and quantity of the available photometry samples. In general, the error source or experimental parameter configuration affecting the L-flat calibration accuracy includes the following types: light source radiation energy correction error; star photometry error; chessboard grid resolution; and photometry sample size. These factors are not independent of each other but contribute to the L-flat calculation results together. Therefore, a simulation model of L-flat calibration for accuracy analysis is established to analyze the influence of these factors quantitatively and provide an estimate of calibration accuracy.

1. Light Source Radiation Energy Correction Error

Our method requires the brightness of the star to be constant; thus, the photoelectric detector at the exit pupil of the collimator is used to correct the output energy variation during the experiment. The photoelectric detector has high monitoring sensitivity and stability, and the stability can be better than 0.1%, indicating that the energy correction error has negligible effects on the calibration accuracy [24].

2. Star Photometry Error

The star photometry error directly affects the accuracy of L-flat extraction. First, the star photometry error in the laboratory is estimated, as determined by the following factors: the shape of star images; detector noise; and stray-light effects. Among them, stray-light effects generally introduce fixed-form noise in the background. Detector noise is introduced from fixed-mode, readout, and dark current noises. According to astronomical data processing experience, most of the above noises can be removed after bias subtraction, detector gain correction, flat field correction, and background subtraction procedures [6,9]. As a result, the shape of star images caused by the diffraction and geometric aberration of the optical system becomes the main factor affecting the photometry error. Given that the space astronomical telescope is a wide FOV diffraction-limited system with competent imaging performance, the following focuses on the influence of the optical path character of the collimator in the calibration equipment on star photometry error. The influence of the support mechanism and material characteristics of the stray-light elimination subassembly are not considered here [25,26].

The simulated optical path of star photometry is shown in Fig. 4. The star light source is placed at the focal plane of the collimator; then, light enters the pupil of the telescope after collimation. The collimator adopts a 2 m F/35 Ritchey–Chrétien type system, whose average RMS wavefront error in the 12 ft × 12 ft FOV is better than 3.67λ ($\lambda = 632.8$ nm; the main components are defocus, tilt, and coma). The telescope is a 2 m F/14 COOK-type three-mirror anastigmatic telescope, in which the average RMS wavefront error in the 12 ft × 12 ft FOV is only 0.05 λ ($\lambda = 632.8$ nm) [27]. The

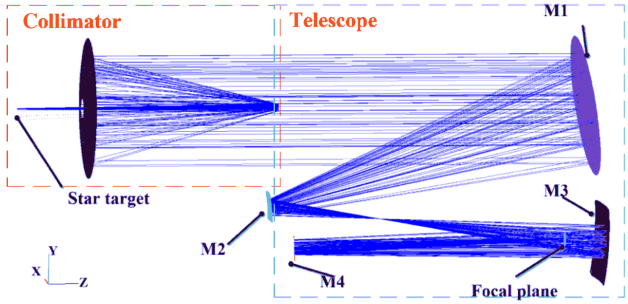

Fig. 4. Simulated optical path of star photometry.

telescope has three power mirrors, i.e., M1, M2, and M3, and a plane mirror M4. Additionally, a detector at the focal plane with 2500 × 2500 pixels (the size of a single pixel is 40 μm) is used.

As noted, most of the noise in the astronomical image can be removed after the preprocessing algorithm, but a small amount of residual noise still remains. The residual noise can be regarded as random noise and obeys the Gaussian distribution. Therefore, Gaussian noise is added to the original noise-free star images obtained by the simulation model to characterize the star images after preprocessing. The Gaussian noise parameters are set to meet the SNR of the star images at 30 dB [28]. The signal levels of the images are set to change in the range of 0–3200 ADU through gain control. The photometry radius is set to 5 FWHM of the star.

First, the star images at the edge FOV of (−4.9 ft, −4.9 ft) whose image quality degrades seriously, are selected for photometry error analysis. Furthermore, the influence of the pinhole size on the results is investigated here. When the brightness at the pinhole is constant, the 2D and partial 3D star images obtained by different pinhole radii R are shown in Fig. 5. The relative error between the measured and real energy values, together with the 80% encircled energy (EE80) radius, are also presented in Fig. 5. Meanwhile, the EE80 radius and photometry error of star images at different pinhole radii R are shown in Fig. 6.

Ideally, according to the imaging amplification relationship, when R ranges from 0.1 to 0.5 mm, the corresponding star radius ranges from 1 to 5 pixels. However, the EE80 radius of the star is 7.62–8.51 pixels, 7.62 pixels when $R = 0.4$ mm, and 8.51 pixels when $R = 0.15$ mm. Evidently, the star is dispersed, and its barycenter is shifted because of the diffraction and aberration of the collimator. When $R = 0.1$ mm, the star is faint and has a maximum photometry error of 5.93%. As R increases, the star energy gradually increases, together with the photometry error and EE80 radius approximately decreasing, and reaches the lowest value when $R = 0.4$ mm. However, as R continues to increase, the photometry error and EE80 radius actually begin to increase (shown in Fig. 6). One reasonable explanation is that the SNR within the photometry circle decreases as the photometry radius increases, although the star energy continues to increase. This result indicates that when the star at the edge FOV is relatively dispersed for realistic applications, the size of the corresponding pinhole should be appropriately expanded.

We also examined the photometry error of other FOVs within the detector. With the pinhole radius set to $R = 0.4$ mm, the star images at 25 different FOVs within the detector are shown in Fig. 7. The results show that the star in the central

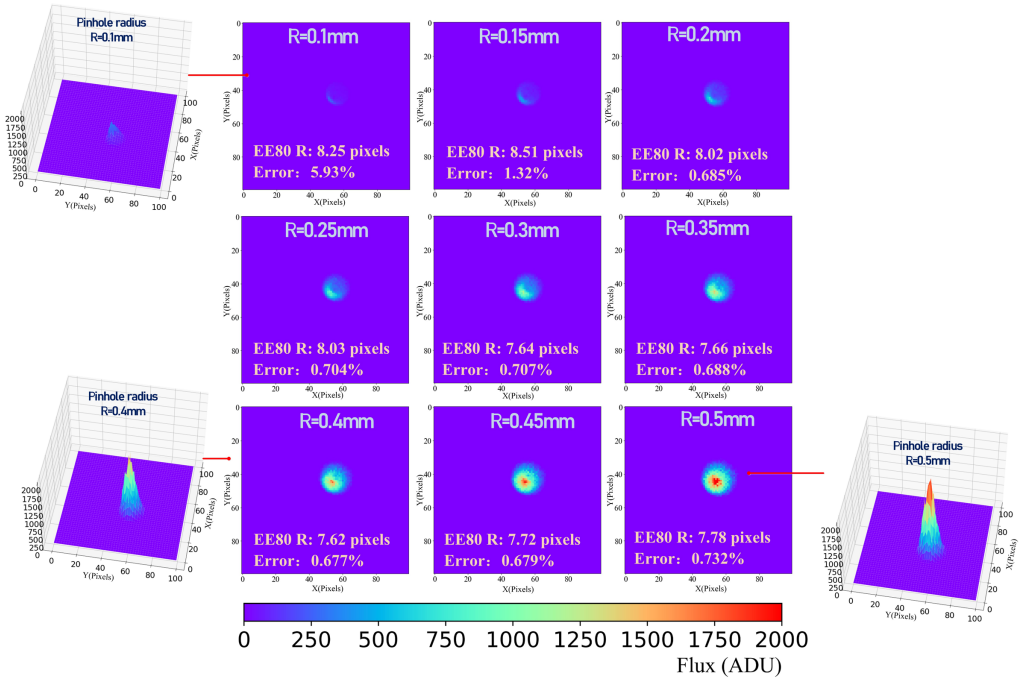

Fig. 5. Shape of star images at FOVs of (−4.9 in., −4.9 ft) obtained by different pinhole radii R.

FOV has the smallest EE80 radius and the highest photometry accuracy. Moreover, the spatial distribution of the star is dispersed as the FOV increases, and the EE80 radius and photometry error reach a maximum at an FOV of (−4.9 ft, 4.9 ft). Thus, image quality degradation leads to a decrease in star energy concentration, which affects the photometry results after superimposing the detector noise. The overall photometry error ranges from 0.15% to 0.72%.

Therefore, when the image quality (here, it refers to the wave aberration) of the collimator at the edge FOV is seriously degraded, the image quality degradation induces photometry error. The overall photometry error range in the 12 ft × 12 ft FOV is approximately 0.15%–0.72%, which to some extent can represent the general level of star photometric error in the laboratory.

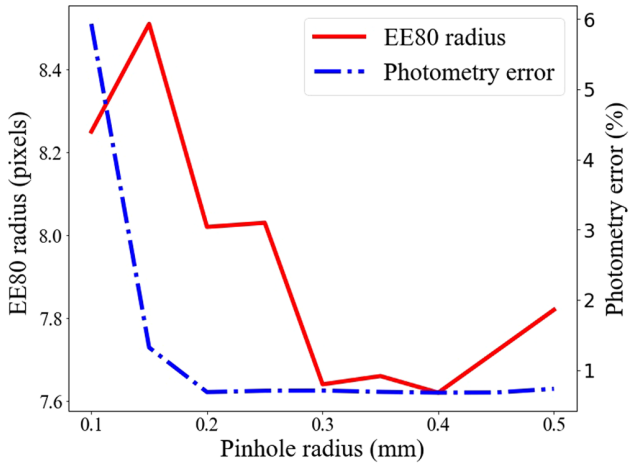

Fig. 6. EE80 radius and photometry error at different pinhole radii R.

Additionally, the influence of star photometry error on L-flat calibration accuracy will be further discussed later via the simulation method.

3. Chessboard Grid Resolution and Photometry Sample Size

As noted, L-flat extraction algorithm obtains the best estimation of L-flat based on numerous photometry samples. Hence, the L-flat calibration accuracy is closely related to the photometry sample size. Additionally, the chessboard basis function is used to characterize the L-flat function. The resolution of the chess board grid determines the ability to distinguish details of the L-flat structure, which also directly affects the L-flat calibration accuracy. Similarly, both factors are discussed in detail in the next section.

4. Simulation Model of L-Flat Calibration

A simulation model is established to analyze quantitatively the influence of the above factors on the accuracy of L-flat calibration. The accuracy of L-flat calibration can be expressed by the difference between the calculated and real L-flat. Given that L-flat denotes the large-scale structure of a flat field, the accuracy of L-flat calibration can be characterized by the absolute value of the maximum deviation of the residual map. The real L-flat is obtained through the artificially generated method. The specific implementation process is as follows: An RMS = 1% reflectivity difference of spatial distribution is added to the telescope mirrors; the main body of the optical system is added with the supporting mechanism and stray-light elimination subassembly that both are coated with uniform black paint with 0.04 reflectivity.

The final real L-flat, which has a final resolution of 2000 × 2000 via the interpolation process, is shown in Fig. 8.

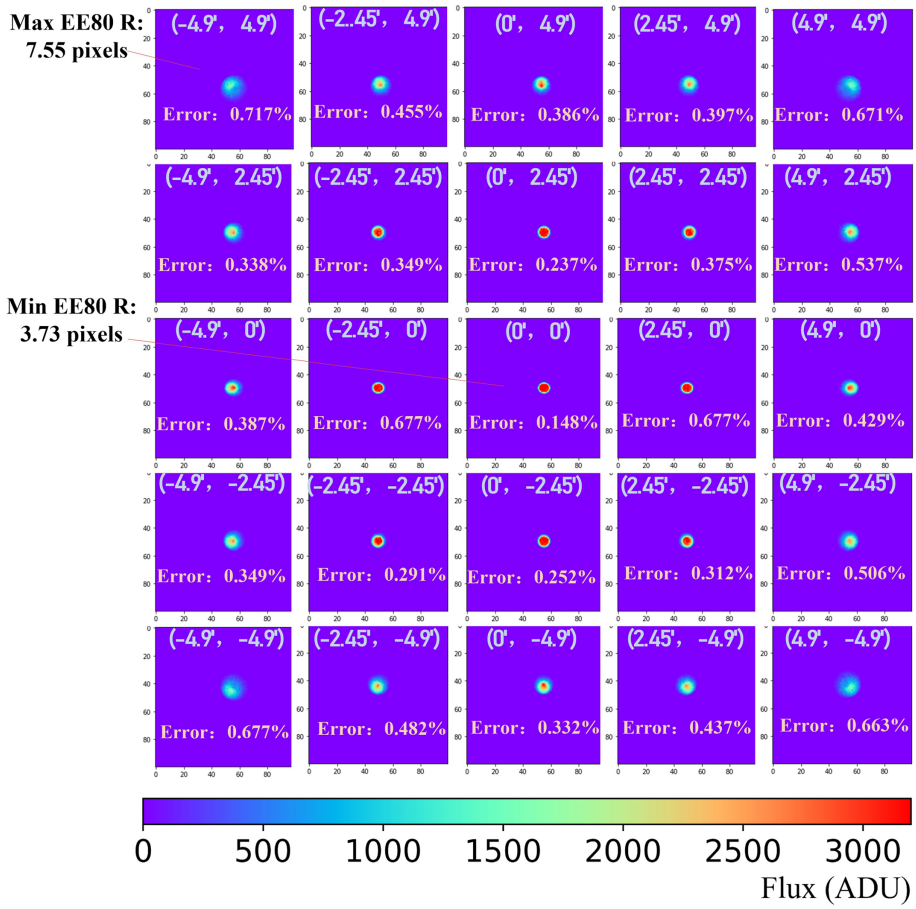

Fig. 7. Star images at 25 different FOVs within the detector.

A gradient structure is present in the left and lower regions, and we suspect that the stray light in the FOV is a potential factor in this phenomenon.

The specific parameter settings of the simulation model are as follows:

1. The detector size is $X \times Y = 2000 \times 2000$, and a total of n stars is uniformly distributed on the detector, where n is set in the range of 100–1500. The corresponding photometry size is in the range of 676–10,302 on account of orientations adjustment.
2. Images are taken at eight additional points, with a step size of 400 pixels from the central point, implying the position of star i in observation sequence j:

$$\begin{cases} x_{ij} = x_{i1} + (-1)^l \times 400, \; l = -1, 0, 1 \\ y_{ij} = y_{i1} + (-1)^n \times 400, \; n = -1, 0, 1 \end{cases} \quad j = 2, 3, \ldots, 9 \tag{7}$$

3. The real flux (F_i) of star i is set at 45,000–55,000 ADU, and the photometry flux (F_{ij}) for observation j of star i fluctuates in the range of $F_i(1 \pm e)$, where e is the star photometry error, with the minimum value of $e_{\min} = 0.15\%$ and maximum value of $e_{\max} = 0.9\%$.
4. The optional chessboard grid resolution is 8×8, 16×16, and 32×32;
5. The measured flux ($O_{i,j}$) using the telescope, which has a real L-flat shown in Fig. 8, is obtained after the combination of the L-flat and the photometry flux:

$$F_{ij} + \text{L-Flat}(x_{ij}, y_{ij}) = O_{ij} \pm e_{ij}, \quad (i = 1, 2, \ldots, N; \; j = 1, 2, \ldots, 9) \tag{8}$$

Next, we investigate the influence of chess board grid resolution on L-flat calibration accuracy. Set $e_{\max} = 0.5\%$ and

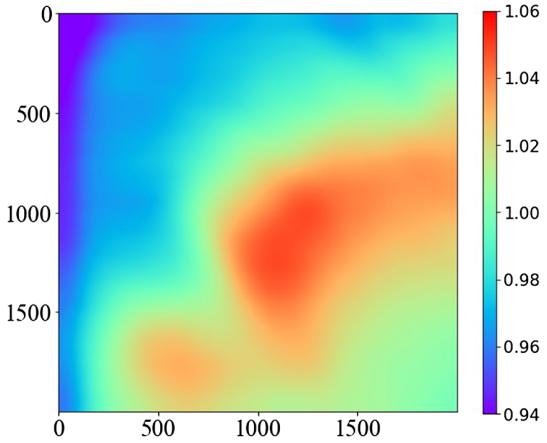

Fig. 8. Real L-flat obtained via the artificial generation method.

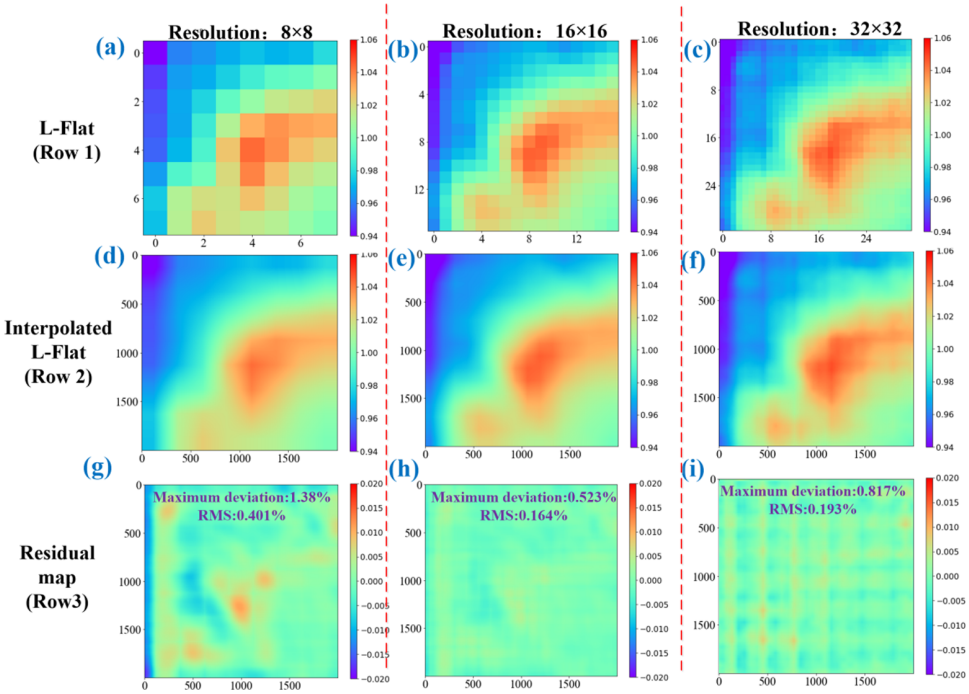

Fig. 9. Results of calculated L-flat using different chessboard grid resolutions. (a)–(c) Initial L-flat calculated from real L-flat using 8 × 8, 16 × 16, and 32 × 32 chessboard grid resolutions, respectively. (d)–(f) Bilinear interpolated L-flats of (a)–(c), respectively. (g)–(i) Residual maps between real L-flat and (d)–(f), respectively.

$n = 1200$. A total of 8,487 photometry records are generated by imaging at different orientations. The resolution of the chessboard grid is set to 8 × 8, 16 × 16, and 32 × 32. The results of the calculated L-flat using different chessboard grid resolutions are shown in Fig. 9.

Given that the resolution of the three initial L-flats (shown in Row 1) obtained by the L-flat extraction algorithm is much lower than that of the real L-flats, bilinear interpolation is thus performed on the initial L-flats (Row 2). The corresponding residual maps between the real and interpolated L-flat are shown in Row 3. The maximum deviation (henceforth referred to as the absolute value) and RMS of residual maps are also shown here. All results capture the essence of the input real L-flat. However, the difference occurs in the narrow strip near the left boundary in Fig. 9(g); that is, when the resolution is relatively low, the L-flat extraction algorithm has a large estimation error in this region. This result indicates that sometimes the relatively larger rectangle size of the grid cannot distinguish and extract the real structure of L-flat with a large gradient. Additionally, fringe patterns appear in Fig. 9(i), indicating that a relatively large estimation error occurs. The number of photometry samples falling on each rectangle is reduced and unevenly distributed with increasing chessboard grid resolution, which directly affects the estimation accuracy in some local regions. In general, the result using a 16 × 16 chessboard resolution is the best and provides a less biased estimate of the true L-flat; the maximum deviation and RMS are 0.523% and 0.164%, respectively. Therefore, a high resolution is not necessarily better; that is, the resolution should match the photometry sample size.

Then, the influence of star photometry error on L-flat calibration accuracy is investigated. The chessboard grid resolution is set to 16 × 16, and the maximum photometry errors are $e_{\max} = 0.3\%$, 0.5%, 0.7% and 0.9%. The maximum deviation and RMS of the residual map, derived by different photometry error settings, are shown as solid lines in Figs. 10(a) and (b), respectively, in which the solid lines with different colors represent different photometry sample sizes. The results show that, when $e_{\max} \leq 0.9\%$, neither the maximum deviation nor the RMS of the residual map shows a clear change trend. Obviously, the photometry accuracy has no considerable effect on the L-flat calibration accuracy. This result also proves that the L-flat extraction algorithm based on the best estimation principle can effectively weaken the influence of star photometry error on the final results.

Furthermore, the influence of the photometry sample size on the L-flat calibration accuracy is investigated. Set $n = 600$, 900, 1200, and 1500, and the corresponding photometry sample sizes are 4212, 6361, 8487, and 10,302. Similarly, the maximum deviation and RMS of the residual map derived by different photometry sample sizes are shown in Figs. 11(a) and (b).

It can be seen that the maximum deviation and RMS of the residual map decrease and tend to stabilize with increasing photometry sample size. Additionally, when the photometry sample size is less than 8487, the result obtained by the 16 × 16 chessboard grid resolution setting is optimal. However, the result of the 32 × 32 resolution becomes slightly better than that of the 16 × 16 resolution when the photometry sample size is 10,302, where the average number of samples for each rectangle is approximately 10 for the 32 × 32 resolution. This result indicates that, when the photometry samples are sufficient, a higher chessboard grid resolution can be selected to

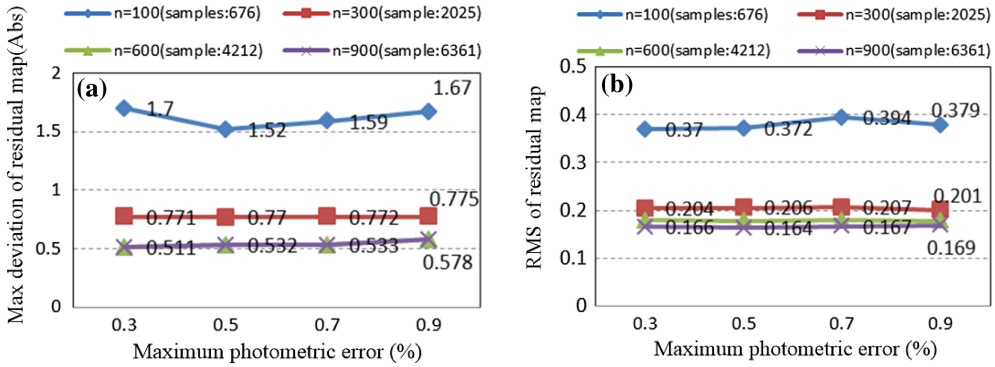

Fig. 10. (a) Maximum deviation and (b) RMS of the residual map derived by different photometry error settings.

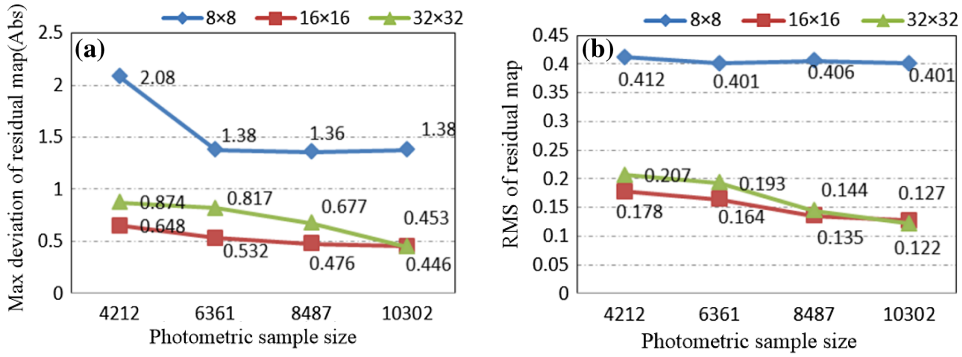

Fig. 11. (a) Maximum deviation and (b) RMS of the residual map derived by different photometry sample sizes. The solid lines with different colors represent different chessboard grid resolutions.

improve the L-flat calibration accuracy. The L-flat calibration accuracy is correlated with the average number of photometry samples falling on the rectangle of the grid. Specifically, when the value is greater than 10, relatively accurate results of L-flat calibration can be ensured. At this time, the maximum deviation of the residual map can reach approximately 0.45%. Overall, the L-flats can be obtained with small random errors, and systematic errors are therefore likely to dominate the true error threshold for realistic applications. However, when the telescope L-flat structure is complex and irregular, the accuracy of the calculated L-flat can be improved to a certain extent by increasing the photometry sample size.

Finally, the L-flat calibration accuracy is estimated. The results of the accuracy analysis show that the maximum deviation of the residual map using our L-flat calibration method can reach 0.45% through reasonable parameter control.

B. Analysis and Discussion of Data Fusion Uncertainty

The data fusion error is the difference between the fused and real flat surfaces. First, the data fusion processing should be analyzed. The flat field is obtained by multiplying L-flat and P-flat in our method; however, the precondition of this operation is that L-flat and P-flat do not overlap in the frequency domain and can reflect the real flat structure in the frequency domain, although the data fusion procedure is implemented in the spatial domain.

On the one hand, P-flat is obtained by detector-wise flat-field calibration, which denotes the pixel-to-pixel radiation response difference of the detector. While L-flat calibration removes the influence of the detector effect during the star image preprocessing procedure, we can rely on the assumption that no small-scale variations occur in L-flat. Furthermore, we can conclude that no overlap exists in the frequency domain. On the other hand, under ideal conditions, when the photometry samples are sufficient, L-flat determines the middle- and large-scale structural characteristics of the real flat surface. At this time, the error introduced by the data fusion procedure is small. In consideration of the complexity of the environment and equipment for realistic measurement, the conservatively estimated data fusion uncertainty is 0.5%.

C. Uncertainty Estimates of the Calibration Method

In summary, the uncertainty sources contributing to the proposed calibration method are shown in Table 1. The final combined uncertainty of the calibration method is 0.78%.

Table 1. Evaluation of Calibration Uncertainty for the Proposed Calibration Method

Uncertainty Source	Uncertainty (%)
L-flat calibration accuracy	0.45
P-flat calculation uncertainty	0.4
Data fusion uncertainty	0.5
Combined uncertainty	0.78

4. EXPERIMENTAL VERIFICATION

A. Experimental Scheme

An experiment was conducted to further illustrate the effectiveness and calibration accuracy of the proposed method. A Nikon lens with a 142 mm aperture, 800 mm focal length, and a visible CCD detector with a 12-bit digital output is used as the telescope in the following experiment. On the basis of the flat-field illumination reference source and the proposed method, the measurement results of the flat field are compared in detail, where a $\Phi = 1.2$ m integrating sphere light source is selected as the flat-field illumination reference source, and the corresponding result is considered the reference flat. The experimental optical paths of the L-flat, P-flat, and reference flat calibration are shown in Figs. 12–14.

Table 2 illustrates the main experimental devices and parameters. These experimental devices consist of a light source, collimator, integrating sphere, shading dark box, and multipinhole mask. For the multipinhole mask, the size of the central pinhole is designed to be slightly larger than that of the others

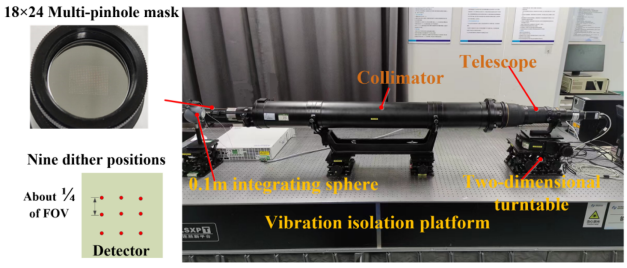

Fig. 12. Experimental optical path of L-flat calibration.

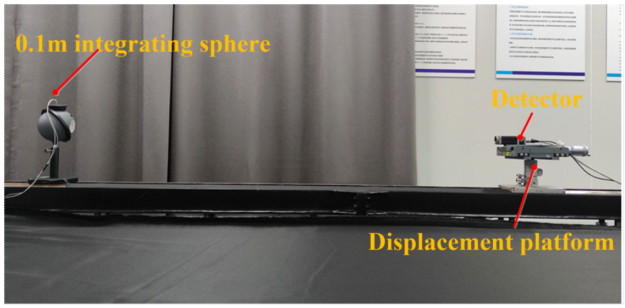

Fig. 13. Experimental optical path of P-flat calibration.

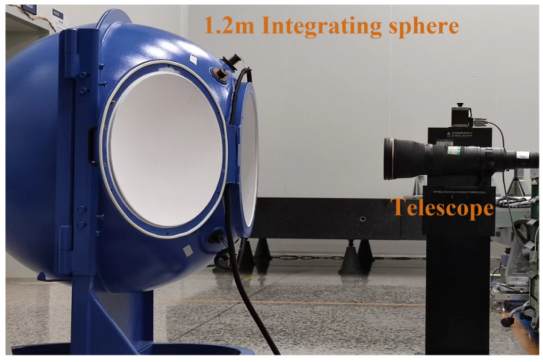

Fig. 14. Experimental optical path of the reference flat calibration.

to identify and mark the stars effectively. Before the experiment, the shaded dark box was placed outside the experimental devices. Meanwhile, all the experimental devices are placed on the vibration isolation platform. For L-flat calibration, to increase the photometry sample size, 18 observations of nine dither positions (3 × 3 grid) are collected using the 2D turntable, with dither steps of ∼25% of the telescope FOV. For P-flat calibration, the spherical orifice of the integrating sphere is set almost parallel to the detector's surface.

Given that the digital-to-analog converter of the detector has a resolution of 12 bits and yields 4096 levels, the average signal levels are controlled at the middle of the converter range level (approximately 2800 ADU), and 12 images are collected for each measurement of the star field at a certain orientations, bias, and flat field. Additionally, the image central region of 1200 × 1600 pixels is selected for data processing and method validation.

Parts of the original star field images are shown in Fig. 15. It can be seen that the size of the central star (shown in Region 3) in Fig. 15(b) is slightly larger than that of the others, and this imaging result is consistent with the structure of the multipinhole mask. Here, the central star is only used for star marking. Furthermore, the star disappeared (shown in Region 4) in Fig. 15(b) due to the etching defect of the multipinhole mask. Therefore, a total of 430 stars participate in star photometry when excluding the central and dark stars, and a total of 6450 photometry samples are finally obtained through orientation adjustment. The FWHM of these stars varies from 3.61 to 4.28 pixels, which is close to the ideal star radius of 3.62 pixels according to the imaging amplification relationship. The star photometry error calculated from Eq. (3) is in the range of 0.319%–0.398%. As an example of the results, two enlarged star images in the center and at the edge FOV in Fig. 15(a) are shown in Figs. 15(c) and (d), and the FWHM is 4.16 and 3.92, respectively. This result indicates that the stars at different positions of the image have relatively consistent imaging quality and contrast.

The normalized reference flat and detector-wise flat are shown in Fig. 16. Some minor bright spots appear in the reference flat due to dust contamination of the Nikon lens group. These bright spots are treated as part of the flat-field structure of the telescope.

The parameter settings for data processing are as follows: the mesh size in the background estimation is 64 pixels, the gain correction coefficient ratio of the left channel to the right channel is 0.971, the star detection threshold is five times the local background standard deviation, and the aperture photometry radius is set to five times the star FWHM. Finally, the observed flux of stars ranges from 41,627 to 57,996 ADU.

Before the analysis of the experimental results, the difference between the simulation model and the verification experiment should be analyzed to ensure the feasibility of the verification experiment. Specifically, for P-flat calibration, the calibration method, device, and data processing in verification are highly consistent with the simulation model mentioned above. Thus, the difference is mainly concentrated in the L-flat calibration procedure. Therefore, the differences in factors affecting the

Table 2. List of Main Experimental Devices and Parameters

Device	Parameter
0.1 m integrating sphere	$\Phi = 100$ mm; spherical orifice: $\Phi = 38$ mm; uniformity: approximately 1%
Light source	OSRAM halogen lamp; electric power: 50 W; stability: <0.1% (1 h)
Collimator	$\Phi = 150$ mm; F − ratio = 10.67; FOV = 0.8°; spectrum transmittance: >80% (450–750 nm)
Multipinhole mask	Etching on chrome-plated glass; $\Phi = 21.5$ mm; 18 × 24 array; hole size: 40; ± 0.5 μm (central), 25 ± 0.5 μm (otherwise)
1.2 m integrating sphere	$\Phi = 1200$ mm; spherical orifice $\Phi = 500$ mm; nonuniformity: approximately 1.21% (within ± 20° FOV)
2D turntable	Azimuth and pitch angle adjustment
Telescope	Nikon AF-S800: $\Phi = 142$ mm; F − ratio = 5.6; CCD detector: Basler pia2400-17gm; pixel size(μm): 3.45; image pixels: 2050 × 2448

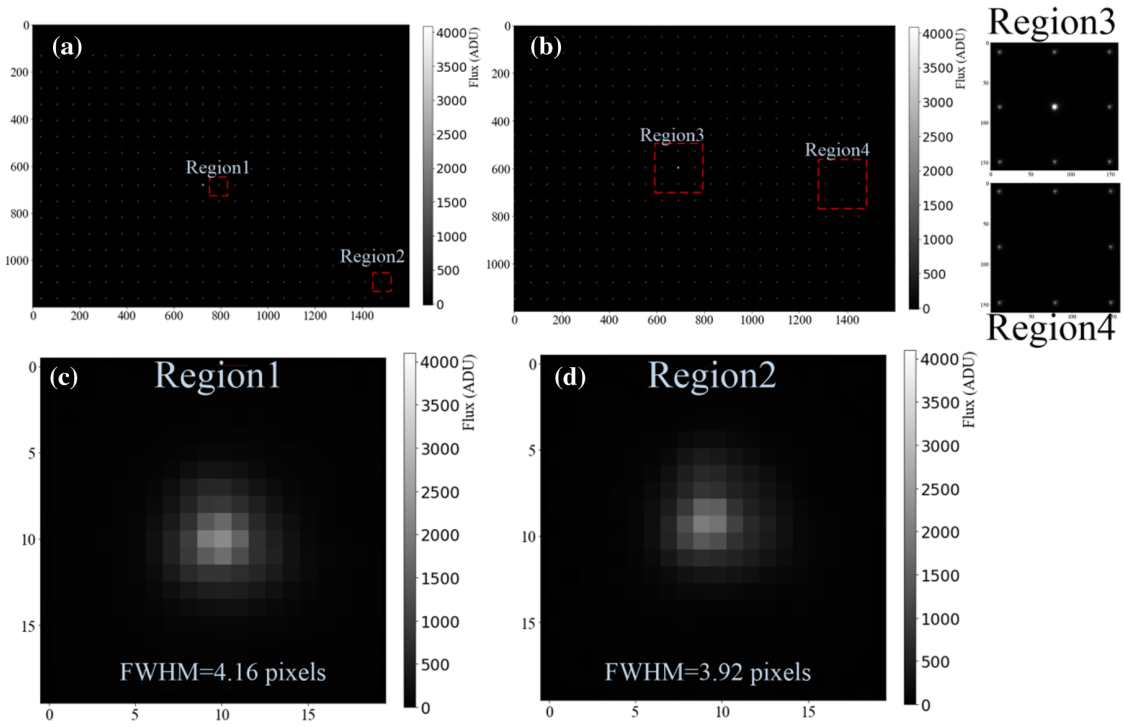

Fig. 15. Part of the original star field images. (a) and (b) Star field images taken at different observation positions. (c) and (d) Enlarged star images of local regions 1 and 2 in (a), respectively.

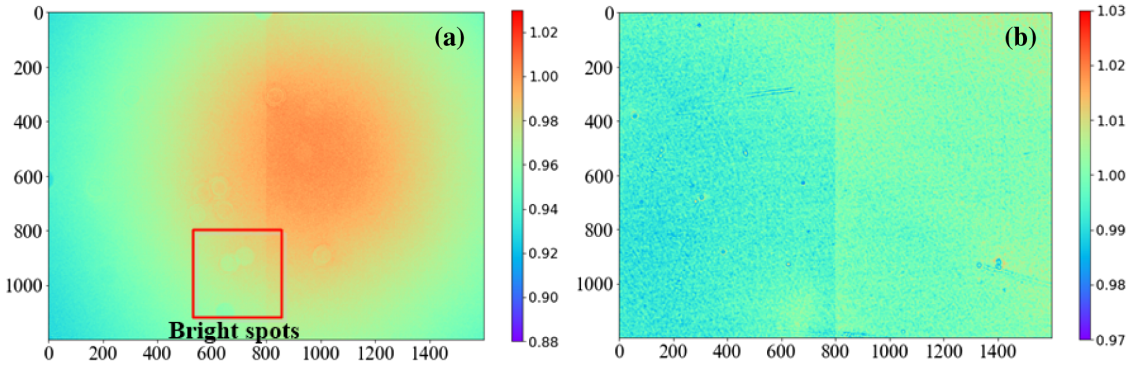

Fig. 16. (a) Normalized reference flat. (b) Detector-wise flat.

L-flat calibration accuracy, that is, the error source or experimental parameter configuration, are discussed in detail below.

1. Light source radiation energy correction error
   Test reports of the halogen lamp show that radiation energy drift in 1 h (the time required for the experiment

to complete the measurement) is approximately 0.1%. Hence, no reference silicon photodiode is used to correct the radiation energy variations in the verification experiment. In this case, the stability of the light source itself represents the light source radiation energy correction error, which is much smaller than the L-flat calibration accuracy. Therefore, the difference in light source radiation energy correction error has negligible effects on the calibration accuracy.

2. Star photometry error
   The results of the star photometry test show that the general level of star photometric error in the laboratory is between 0.15% and 0.72%. Furthermore, the accuracy analysis results of L-flat calibration show that, when the star photometry error is less than 0.9%, it has no remarkable effect on L-flat calibration accuracy. Given the smaller aperture and larger FOV of the optical system used in the verification experiment, we first need to confirm the error range of star photometry. Fortunately, the results of star photometry in the verification experiment show that the relative photometry error calculated with Eq. (1) is in the range of 0.319%–0.398%, which is within the range of results at the star photometry test and consistent with the simulation model of L-flat calibration.
3. Chessboard grid resolution and photometry sample size
   Eighteen observations at nine orientations are adopted in the experiment, and 6450 photometry samples are finally obtained; this number is close to the photometry sample size in the simulation model. Additionally, the chessboard grid resolutions selected in the verification experiment are 9×12, 18×24, and 30×40 to ensure that the number of rectangles of the grid is at the same level as the simulation model.

In summary, the difference between the simulation model and the verification experiment in the error source and experimental parameter configuration does not theoretically affect the final calibration results.

B. Results

The results of the calculated L-flat at different chessboard grid resolutions are shown in Fig. 17. Bright spots are present in the marked region in Figs. 17(b) and (c), indicating the following: On the one hand, the L-flat extraction algorithm reconstructs the flat field structure caused by dust contamination of the Nikon lenses group well; on the other hand, the improved grid resolution considerably enhances the detailed representation capability of L-flat. Meanwhile, abnormal data appear in some rectangles at the bottom boundary in Fig. 15(c). According to the photometry sample size and chessboard grid resolution, the average number of samples involved in a rectangle of grid is only 5.375. Moreover, this value at the boundary rectangles would be less than or even zero, leading to a large deviation in the L-flat calculation.

Next, L-flat with a resolution of 18×24 is used for bilinear interpolation and data fusion, and the calculated flat is obtained. Then, a comparison between the calculated and reference flats is shown in Fig. 18. Figures 18(a) and (b) show that the overall structure is consistent, and the corresponding residual map, shown in Fig. 18(c), shows no evident large-scale structure. However, slight discontinuity is still observed in the local region of Fig. 18(b), which is related to the relative independence of each rectangle of the chessboard grid. The accuracy of the results can be improved considerably through the application of additional smoothing. However, this also smooths away the intermediate-frequency structure, which is actually present in the real L-flat. Additionally, the optimum amount of smoothing depends on the frequency content of the real L-flat, which in practice is not known. Hence, smoothing processing is not here. Apart from the noise and obvious "pixelization" of the residual map, the absolute value of maximum deviation in the residual map is 2.86%.

To evaluate the difference between the calculated and reference flats comprehensively, the residual map RMS at different scales is investigated: small-, middle-, and large-scale RMS [29]. These values can be obtained by calculating the average RMS of each 100×100, 400×400, and 1200×1600 pixels in the residual map. The results are as follows: RMS1 = 0.558%; RMS2 = 0.565%; and RMS3 = 0.720%. In general, the RMS of different scales are relatively close, and RMS3 is the largest, which indicates that the large-scale difference is still the main component and contributes the most to the flat field calibration error. The approximately linear gradient between the top left and bottom right in Fig. 17(c) likely leads to the tiny large-scale difference. Definitely, the L-flat calibration accuracy depends on the quality and quantity of the available photometry samples and on the properties of the L-flat. The remaining small L-flat calibration systematic errors therefore dominate the true error threshold for the verification experiment.

To avoid accidental results, three experiments were conducted under the same conditions. Here, the chessboard grid resolution of 18×24 is chosen for comparison. Overall, all the results of the three experiments look the same and are visually indistinguishable from each other; thus, they are not shown here. Table 3 presents the maximum deviation and RMS of the

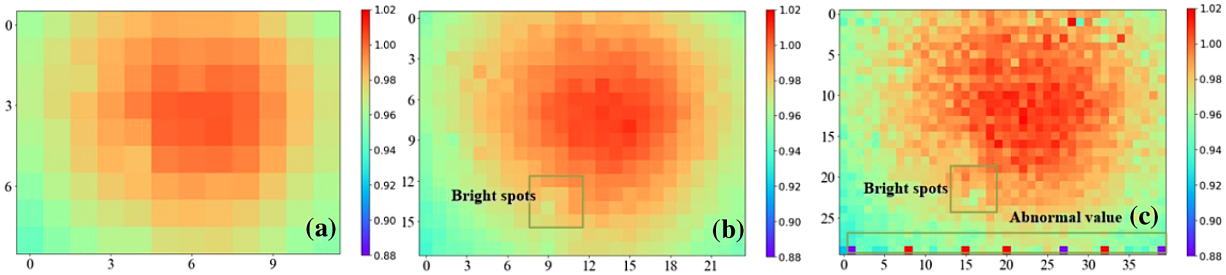

Fig. 17. Results of calculated L-flat by using different chessboard grid resolutions. (a) Resolution: 9×12. (b) Resolution: 18×24. (c) Resolution: 30×40.

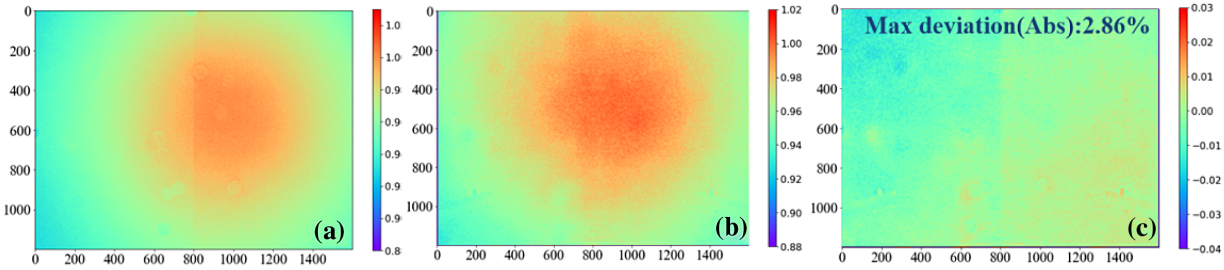

Fig. 18. Comparison between the reference and calculated flat surfaces. (a) and (b) Reference and calculated flat, respectively. (c) Residual map between them.

Table 3. Summary of Maximum Deviation and RMS of the Residual Map

Serial Number	Maximum Deviation of Residual Map (%)	RMS of Residual Map (%)		
		RMS1	RMS2	RMS3
1	2.86	0.558	0.565	0.720
2	2.89	0.564	0.559	0.726
3	2.83	0.586	0.588	0.701

residual map derived from the experiments. Repeated experiments show that the calibration method and algorithm work well and verify the stability and effectiveness of the calibration method.

C. Analysis and Discussion of the Calibration Accuracy

This section aims to assess the calibration uncertainty of the proposed method in the experiment. Calibration uncertainty is mainly introduced in two parts. One is the uncertainty of the integrating sphere light source, which is mainly determined by the uniformity and Lambert characteristics of the spherical orifice. The other is the difference between the calculated and reference flats, which is characterized by the RMS of the residual map.

Calibration reports of the 1.2 m integrating sphere show that the nonuniformity of the integrating sphere is 1.21%. Specifically, the spatial nonuniformity (within $\Phi = 0.5$ m) of the integrating sphere is 0.33%, and the angular nonuniformity (within $\pm 20°$) is 1.17%. Given that only the central area and FOV of the integrating light source are used to obtain the reference flat, this ensures that the accuracy of flat calibration is better than $\pm 0.5\%$. Additionally, according to the results of the three experiments shown in Table 3, the maximum RMS of the residual map is 0.726%. Therefore, the total uncertainty of the proposed method is 0.88%, which is close to the result of the accuracy analysis (0.78%).

The key to the calibration method in this study is the data processing algorithm rather than the calibration equipment. Hence, this method can be applied to conventional calibration equipment. For example, the L-flat extraction algorithm based on the optimal estimation principle can weaken the influence of photometry accuracy and thus greatly reduce the requirements for collimator and light source uniformity. This characteristic of the method also leads to a high agreement between the accuracy analysis results and the experimental results. However, the verification experiment also shows that the system error of L-flat calibration still exists, and potential factors, such as the temperature fluctuation of the detector, airflow, and vibration, all affect the verification experiment.

5. CONCLUSION

With the increasing telescope aperture, the manufacturing cost and difficulty of the flat-field illumination reference source covering the FOV and aperture of the telescope increase sharply, directly resulting in a considerable decrease in ground flat-field calibration accuracy. The spatial time-sharing calibration method in this study can independently obtain two spatial scale flat fields, and the final flat field is derived through a spatial data fusion procedure. Specifically, L-flat is extracted by star field observations and the corresponding L-flat extraction algorithm based on the optimal estimation principle. This method cannot only eliminate the restriction of flat-field illumination reference sources but also increase the accuracy of flat-field calibration from the perspective of data processing to be widely applied in the area of ground flat-field calibration. The simulation model for accuracy analysis is established, and the influence of each error source or experimental parameter configuration on the L-flat calibration accuracy is analyzed in detail. The calibration method is verified by conducting experiments. The following conclusions can be drawn from this study:

1. Star photometry error is mainly affected by pinhole size and the optical path character of the collimator. For the star images at the edge FOV of the collimator, a pinhole size that is too small leads to a decrease in the energy concentration and signal level, which affects the photometric results after superimposing the detector noise. The overall photometry error in the 12 ft × 12 ft FOV ranges from 0.15% to 0.72%.
2. When star photometry error $e \leq 0.9\%$, neither maximum deviation nor RMS shows a clear change trend. This trend indicates that the L-flat extraction algorithm based on optimal estimation can effectively weaken the influence of photometry accuracy. Second, the proposed method has low requirements for calibration equipment, such as a collimator, multihole mask, and integrating sphere light source, which make the method flexible in practical applications.
3. When the photometry sample size is fixed, a relatively large estimation error occurs in the local region with increasing chessboard grid resolution. Therefore, high resolution is

not necessarily better; that is, the resolution should match the photometry sample size.

4. According to the experience of simulation analysis and verification experiments, when the average number of photometry samples for each grid "pixel" is greater than 10, the calculation results are likely to be more accurate.
5. The accuracy of L-flat calibration decreases and tends to stabilize with increasing photometry sample size. Therefore, L-flats can be obtained with small random errors, and systematic errors are therefore likely to dominate the true error threshold for realistic applications.
6. The good coincidence between the experimental results and the simulated results demonstrates that the simulation model of accuracy analysis is reasonable, and the proposed method is feasible. The calibration accuracy of the proposed method is better than the general accuracy of the ground flat field calibration of the astronomical telescope.
7. It is worth noting, however, that some limitations of the collimator to the proposed method cannot be ignored. First, the aperture of the collimator needs to match that of the telescope. Second, for some wide-diffraction-limited FOV telescope, the FOV of the collimator may be limited. At this time, more orientation adjustments are required to realize the coverage of the telescope's FOV.

Funding. National Natural Science Foundation of China (12003033); National Key Research and Development Program of China (2021YFC2802100); Youth Innovation Promotion Association of the Chinese Academy of Sciences (2023225).

Disclosures. The authors declare no conflicts of interest.

Data availability. Data underlying the results presented in this paper are not publicly available at this time but may be obtained from the authors upon reasonable request.

REFERENCES

1. T. D. Rawle, C. Alves de Oliveira, S. M. Birkmann, T. Boeker, G. de Marchi, P. Ferruit, G. Giardino, N. Luetzgendorf, and M. Sirianni, "Flat-fielding strategy for the JWST/NIRSpec multi-object spectrograph," Proc. SPIE **9904**, 990446 (2016).
2. J. Anderson, L. R. Bedin, G. Piotto, R. S. Yadav, and A. Bellini, "Ground-based CCD astrometry with wide field imagers-I. Observations just a few years apart allow decontamination of field objects from members in two globular clusters," Astron. Astrophys. **454**, 1029–1045 (2006).
3. R. Laureijs, J. Amiaux, S. Arduini, J.-L. Augueres, J. Brinchmann, R. Cole, M. Cropper, C. Dabin, L. Duvet, and A. Ealet, "Euclid definition study report," arXiv, arXiv:1110.3193 (2011).
4. J. Mack, E. Sabbi, and T. Dahlen, "In-flight corrections to the WFC3 UVIS flat fields," Instrument Science Report WFC3 2013-10 (2013).
5. R. P. van der Marel, "Determination of low-frequency flat-field structure from photometry of stellar fields," Instrument Science Report ACS 2003-10 (2003).
6. B. Dorner, G. Giardino, P. Ferruit, C. A. de Oliveira, S. M. Birkmann, T. Böker, and P. Jakobsen, "A model-based approach to the spatial and spectral calibration of NIRSpec onboard JWST," Astron. Astrophys. **592**, A113 (2016).
7. K. M. Vogelhuber, K. Fulford, R. Serafico, D. Turpen, R. Cooper, and S. Schieffer, "General methods for the characterization of the nonuniformity of a radiometric calibration source," Appl. Opt. **58**, 4918–4925 (2019).
8. Z. Sun, S. Chang, and W. Zhu, "Radiometric calibration method for large aperture infrared system with broad dynamic range," Appl. Opt. **54**, 4659–4666 (2015).
9. C. W. Stubbs and J. L. Tonry, "Toward 1% photometry: End-to-end calibration of astronomical telescopes and detectors," Astrophys. J. **646**, 1436 (2006).
10. S. Gogler, G. Bieszczad, J. Swiderski, K. Firmanty, J. Bareła, and T. Piątkowski, "Fast and accurate polarimetric calibration of infrared imaging polarimetric sensors," Appl. Opt. **60**, 8499–8512 (2021).
11. J. P. Rheault, D. L. DePoy, J. L. Marshall, T. Prochaska, R. Allen, J. Wise, and P. Williams, "Spectrophotometric calibration system for DECam," Proc. SPIE **8446**, 1953–1961 (2012).
12. C. W. Stubbs, P. Doherty, C. Cramer, G. Narayan, Y. J. Brown, K. R. Lykke, and J. L. Tonry, "Precise throughput determination of the PanSTARRS telescope and the gigapixel imager using a calibrated silicon photodiode and a tunable laser: initial results," Astrophys. J. Suppl. Ser. **191**, 376 (2010).
13. J. Mack, R. Bohlin, R. Gilliland, R. Van Der Marel, J. Blakeslee, and G. De Marchi, "ACS L-flats for the WFC," Instrument Science Report ACS 2002-2008 (2002).
14. M. W. Coughlin, S. Deustua, A. Guyonnet, N. Mondrik, J. P. Rice, C. W. Stubbs, and J. T. Woodward, "Testing of the LSST's photometric calibration strategy at the CTIO 0.9 meter telescope," Proc. SPIE **10704**, 753–765 (2018).
15. J. Bosch, Y. AlSayyad, R. Armstrong, E. Bellm, H. F. Chiang, S. Eggl, and W. M. Wood-Vasey, "An overview of the LSST image processing pipelines," arXiv, arXiv:1812.03248 (2018).
16. M. Coughlin, T. M. C. Abbott, K. Brannon, C. Claver, P. Doherty, M. Fisher-Levine, and C. Stubbs, "A collimated beam projector for precise telescope calibration," Proc. SPIE **9910**, 276–285 (2016).
17. J. E. Van Cleve and D. A. Caldwell, "Kepler instrument handbook," Kepler Science Document KSCI-19033-002, 1 (2016).
18. E. V. Quintana, J. M. Jenkins, B. D. Clarke, H. Chandrasekaran, J. D. Twicken, S. D. McCauliff, and S. T. Bryson, "Pixel-level calibration in the Kepler Science Operations Center pipeline," Proc. SPIE **7740**, 697–708 (2010).
19. D. A. Caldwell, J. J. Kolodziejczak, J. E. Van Cleve, J. M. Jenkins, P. R. Gazis, V. S. Argabright, E. E. Bachtell, E. W. Dunham, J. C. Geary, R. L. Gilliland, H. Chandrasekaran, J. Li, P. Tenenbaum, H. Wu, W. J. Borucki, S. T. Bryson, J. L. Dotson, M. R. Haas, and D. G. Koch, "Instrument performance in Kepler's first months," Astrophys. J. Lett. **713**, L92 (2010).
20. M. D. Lallo, "Experience with the Hubble Space Telescope: twenty years of an archetype," Opt. Eng. **51**, 011011 (2012).
21. P. Jakobsen, P. Ferruit, C. A. de Oliveira, S. Arribas, G. Bagnasco, R. Barho, and C. Zincke, "The near-infrared spectrograph (NIRSPEC) on the James Webb space telescope-I. Overview of the instrument and its capabilities," Astron. Astrophys. **661**, A80 (2022).
22. E. Bertin and S. Arnouts, "SExtractor: Software for source extraction," Astron. Astrophys. **117**, 393–404 (1996).
23. E. Merlin, S. Pilo, A. Fontana, M. Castellano, D. Paris, V. Roscani, and M. Torelli, "A-PHOT: a new, versatile code for precision aperture photometry," Astron. Astrophys. **622**, A169 (2019).
24. N. Regnault, A. Guyonnet, K. Schahmaneche, L. Le Guillou, P. Antilogus, P. Astier, and F. Villa, "The DICE calibration project design, characterization, and first results," Astron. Astrophys. **581**, A45 (2015).
25. Y. Luo, Z. Feng, Y. Han, and H. Li, "Design of compact and smooth freeform optical system with uniform illuminance for LED source," Opt. Express **18**, 9055–9063 (2010).
26. Y. Jiang, J. Tian, W. Fang, D. Hu, and X. Ye, "Freeform reflector light source used for space traceable spectral radiance calibration on the solar reflected band," Opt. Express **31**, 8049–8067 (2023).
27. F. Zeng, X. Zhang, J. Zhang, G. Shi, and H. Wu, "Optics ellipticity performance of an unobscured off-axis space telescope," Opt. Express **22**, 25277–25285 (2014).
28. M. Riello, F. D. Angeli, D. W. Evans, G. Busso, N. C. Hambly, M. Davidson, P. W. Burgess, P. Montegriffo, P. J. Osborne, A. Kewley, J. M. Carrasco, C. Fabricius, C. Jordi, C. Cacciari, F. Leeuwen, and G. Holland, "Gaia Data Release 2-Processing of the photometric data," Astron. Astrophys. **616**, A3 (2018).
29. F. L. Goerner, T. Duong, R. J. Stafford, and G. D. Clarke, "A comparison of five standard methods for evaluating image intensity uniformity in partially parallel imaging MRI," Med. Phys. **40**, 082302 (2013).